Astron. Astrophys. 321, 945–959 (1997)

ASTRONOMY
AND
ASTROPHYSICS

Solar wind velocity jumps across tangential discontinuities: Ulysses observations and kinetic interpretation

J. De Keyser[1], **M. Roth**[1], **B.T. Tsurutani**[2], **C.M. Ho**[2], **and J.L. Phillips**[3]

[1] Belgian Institute for Space Aeronomy, Ringlaan 3, B-1180 Brussels, Belgium
[2] Jet Propulsion Laboratory, California Institute of Technology, Pasadena, CA 91109, USA
[3] Los Alamos National Laboratory, Los Alamos, NM 87545, USA

Received 17 May 1996 / Accepted 24 October 1996

Abstract. Some tangential discontinuities (TDs) observed by the ULYSSES spacecraft interface solar wind regions that differ only in their bulk velocity and magnetic field orientation; composition, density, temperature and magnetic field intensity are essentially the same in both regions. The relation between the plasma velocity jump across the TD and the magnetic field is investigated through the analysis and simulation of equilibrium plane TD configurations. These theoretical results are compared with ULYSSES observations. It is concluded that (a) the theoretically predicted magnetic field profile agrees with the morphology of the observed profile, (b) solar wind transitions are essentially of mixed type, i.e. both ion and electron velocity distribution functions are non-Maxwellian inside the transition layer, (c) there are constraints on the orientation and magnitude of the velocity jump that can be supported across a single transition, (d) large magnetic field rotations correspond to wide transition layers, and (e) in addition to density and temperature inhomogeneities, variations in the bulk velocity are a major reason for the solar wind plasma to set up current-carrying boundary layers.

Key words: magnetic fields – plasmas – solar wind – interplanetary medium

1. Introduction

When two magnetized solar wind plasmas interact, they set up a narrow interfacing layer, a so-called plasma discontinuity. Such a layer typically has a thickness determined by the representative ion gyroradius. Within this layer the velocity distribution functions may deviate significantly from Maxwellians. A kinetic description, rather than an MHD one, is therefore appropriate. Different types of plasma discontinuities exist, as can be derived from the Rankine-Hugoniot relations (Hudson 1971). Tangential discontinuities (TDs) are equilibrium configurations that are characterized by vanishing normal magnetic field component and normal velocity. There is no net mass flux across the transition.

TDs are a common phenomenon in the solar wind. A number of statistical studies of TDs have been carried out, mainly in the ecliptic plane (Burlaga et al. 1977; Tsurutani & Smith 1979; Behannon et al. 1981), but recently also at high heliographic latitudes using ULYSSES observations (Tsurutani et al. 1994; Ho et al. 1995). These investigations quantify the rate of occurrence of TDs and their macroscopic properties such as thickness and magnetic field rotation angle. The microscopic internal structure of solar wind TDs has been the subject of a few kinetic studies (Lemaire & Burlaga 1976; Roth 1986; De Keyser et al. 1996).

Solar wind TDs are known to occur throughout the inner heliosphere. Observations of the heliospheric current sheet (HCS) sometimes reveal a TD structure. Its thickness may exceed 100 proton gyroradii (Behannon et al. 1981). Other structures with which TDs may be associated include noncompressive density enhancements (Gosling et al. 1977). There, the TDs separate a distinct plasma entity with higher density and lower temperature from the surrounding solar wind environment. TDs associated with such large scale events may have distinct properties that differentiate them from the TDs commonly observed in the background solar wind (Lepping & Behannon 1986); they will therefore not be addressed here. In their recent study of TDs in the polar solar wind, Ho et al. (1995) distinguish two types of TDs: (a) mirror-mode structures, characterized by variations in magnetic field intensity without appreciable field rotation, often occurring in pairs, that are associated with high proton temperature anisotropies, and (b) current-sheet-associated TDs, characterized by significant variations in magnetic field magnitude and orientation, plasma density and temperature, that are associated with solar wind velocity jumps. In this paper, a class of solar wind TDs is investigated that resembles the latter case: only TDs that are accompanied by a plasma velocity jump and a certain magnetic field rotation are considered, while the other plasma parameters remain essentially constant.

Send offprint requests to: J. De Keyser

This paper first discusses observations for a few typical TDs belonging to this class. Next, a kinetic equilibrium model for such transitions is outlined. Attention is paid to the role of the velocity jump: an equilibrium configuration appears to exist only when the relative velocity obeys certain criteria. The model is then applied to simulate the internal structure of the observed transitions. Finally, some conclusions are drawn that apply to this class of solar wind TDs, but that may be valid in a wider context as well.

2. Observations

Solar wind TDs usually are assumed to be locally planar, i.e. the radius of curvature of the TD is much larger than the typical ion gyroradius. This assumption is widely accepted as a working hypothesis, although it is inherently impossible to validate it experimentally using single-spacecraft observations. The planarity assumption is consistent with the interpretation of current-sheet-associated TDs as being the interface between solar wind streams flowing outward from the Sun at slightly different velocities, as suggested by Ho et al. (1995).

In order to avoid confusion with TD transitions of the HCS, only high heliolatitudes were considered. TDs are identified based on magnetic field observations with high time resolution. In order not to bias the TD selection process, the time resolution should be such that the corresponding spatial resolution (in the direction normal to the TD plane) is better than one proton gyroradius, as solar wind TDs are mainly ion-dominated or mixed transitions, whose minimum thickness is the ion gyroradius (Sestero 1964). The ULYSSES high time resolution magnetometer data (1 or 2 vectors/s) satisfy this criterium; they do so especially for the weak magnetic fields and correspondingly large gyroradii encountered at 2.4–5 AU, in the post-jovian encounter and south polar pass phase of the mission, from which the examples in this paper are taken. Minimum variance analysis is used to distinguish between tangential and rotational discontinuities, based on the magnitude of the normal magnetic field. In practice, a residual normal component is always present; the term "tangential discontinuity" is therefore used here as synonymous to "directional discontinuity with small normal field component".

The time resolution of the plasma data is much lower than that of magnetic field data: the ULYSSES ion spectrometer returns 3-dimensional spectra every 4 to 8 minutes, while the electron instrument returns either 2- or 3-dimensional spectra every 5 to 11 minutes (Bame et al. 1992). A plasma bulk velocity measurement is obtained by gathering data over a time span of 2 minutes, of the order of the usual duration of the passage of a TD. It should be stressed that estimates for the transition width and the relative velocity between the plasmas on either side of the TD may be quite rough and should be used with caution for the following reasons:

1. Often the magnetic field varies strongly in only one direction, so that the TD normal as derived from the minimum variance analysis may be ill-determined. A small error in the normal direction may lead to a substantial error in the normal velocity of the TD in the minimum variance frame (MVF), and hence in the transition width estimate.
2. Considering the velocity difference may eliminate possible systematic errors in the plasma velocity measurements; the uncertainty on the relative velocity is expected to be of the order of a few km s^{-1}.
3. The plasma velocity measurements usually are not made at the very edges of the transition, but may be minutes away. Even when the magnetic field does not exhibit major variations between the points of measurement and the transition, the plasma velocity may vary gradually during these intervals. The true relative velocity is therefore expected to be smaller than the one inferred from the data taken at some distance of the TD.

When trying to relate the relative velocity to the observed magnetic field variations, one should keep this uncertainty in the relative velocity data in mind.

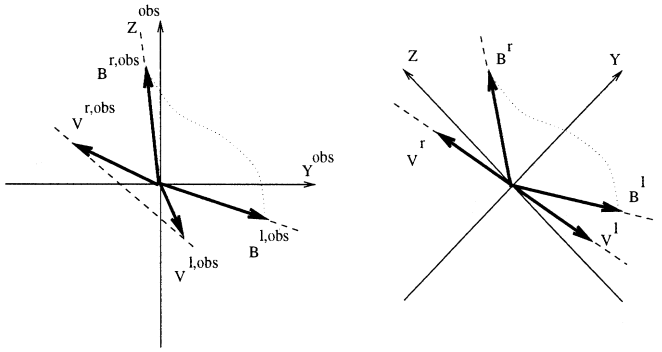

Fig. 1. General configuration considered in this paper. The left panel shows the magnetic field $\boldsymbol{B}^{\rm obs}$ and plasma bulk velocity $\boldsymbol{V}^{\rm obs}$ on the left (l) and right (r) side of the transition in the minimum variance frame ($Y^{\rm obs}$, $Z^{\rm obs}$). The right panel displays the same configuration after a Galilean transformation to the (Y, Z) frame moving with velocity $(\boldsymbol{V}^{\rm l,obs} + \boldsymbol{V}^{\rm r,obs})/2$, rotated such that the Y axis is the inner bisectrix of the two magnetic field vectors.

2.1. Configuration

The following macroscopic observables are derived from the ULYSSES observations: the magnetic field vectors $\boldsymbol{B}^{\rm l,obs}$ and $\boldsymbol{B}^{\rm r,obs}$ on the left and right sides of the TD, the plasma bulk velocities $\boldsymbol{V}^{\rm l,obs}$ and $\boldsymbol{V}^{\rm r,obs}$, and the densities and temperatures far from the transition. The magnetic field intensity on both sides is $B^{\infty} = B^{\rm l} = B^{\rm r}$. The angle between both magnetic field vectors is θ; the angle ω traced by the tip of the magnetic field vector as it rotates from $\boldsymbol{B}^{\rm l,obs}$ to $\boldsymbol{B}^{\rm r,obs}$ might in principle differ from θ by a number of times 360°. The magnetic field variation is $\Delta\boldsymbol{B} = \boldsymbol{B}^{\rm r,obs} - \boldsymbol{B}^{\rm l,obs}$; the relative velocity is defined by $\boldsymbol{V}_{\rm r} = \boldsymbol{V}^{\rm r,obs} - \boldsymbol{V}^{\rm l,obs}$. This configuration is depicted in Fig. 1.

Let the TD plane in the MVF be denoted by ($Y^{\rm obs}$, $Z^{\rm obs}$). The reference frame (Y, Z) best suited for carrying out the kinetic analysis is obtained by means of a Galilean transformation: let the frame move with a constant non-relativistic velocity

$\boldsymbol{V}_{\rm fr} = (\boldsymbol{V}^{\rm l,obs} + \boldsymbol{V}^{\rm r,obs})/2$. The Y axis is oriented along the inner bisectrix of $\boldsymbol{B}^{\rm l,obs}$ and $\boldsymbol{B}^{\rm r,obs}$. One obtains the following symmetries: $\boldsymbol{V}^{\rm r} = -\boldsymbol{V}^{\rm l} = \boldsymbol{V}_{\rm r}/2$, $B^{\rm r}_Z = -B^{\rm l}_Z = B^{\infty}_Z$ and $B^{\rm r}_Y = B^{\rm l}_Y = B^{\infty}_Y$. The Galilean transformation does not affect the magnetic field vectors. It does, however, introduce an additional electric field $\boldsymbol{E}_{\rm fr}(X) = \boldsymbol{V}_{\rm fr} \times \boldsymbol{B}(X)$.

In the local frames of reference moving with the left resp. right plasma, the electrostatic potential ϕ tends to a constant asymptotic value. It is assumed that both constants have the same value. The arbitrary constant in the definition of ϕ is chosen such that this value is zero.

2.2. Event I

The magnetic field profile for the first event is shown in Fig. 2a, with 2 s resolution. ULYSSES encountered this TD on July 3, 1993, $11^{\rm h}40^{\rm m}$ UT, at 4.57 AU and $-33\overset{\circ}{.}85$ heliographic latitude. This encounter took place shortly after the last HCS crossing following the Jupiter fly-by. The high speed solar wind flows at 810 km s^{-1}. The background magnetic field is $B^{\infty} = 0.56$ nT; due to the large heliocentric distance this is quite small, implying a large thermal gyroradius for the 17.2 eV (200 000 K) protons: $\rho^{+} = 1070$ km. The proton density is $N^{\rm p} = 0.13$ cm^{-3}, and fairly uniform in the surrounding solar wind plasma. The thermal proton velocity is $V^{+}_{\rm th} = 57$ km s^{-1}. The electron temperature is measured to be $T^{\rm e} = 47\,000$ K (4.1 eV). The alpha particle density is $N^{\alpha} = 0.005$ cm^{-3}; their temperature is $T^{\alpha} = 780\,000$ K (68 eV). As their mass and temperature both are about 4 times higher than that of the protons, they have the same thermal velocity and a gyroradius twice as large. The plasma beta is $\beta \approx 2\mu_0 k[N^{\rm p}T^{\rm p} + N^{\alpha}T^{\alpha} + (N^{\rm p} + 2N^{\alpha})T^{\rm e}]/(B^{\infty})^2 = 4.03$.

The angle between the TD normal and the solar wind speed is 53°; the normal component of the spacecraft velocity with respect to the TD plane is 490 km s^{-1}. Due to the large gyroradius, the resolution of the internal structure in the TD is pretty good. It took about 200 s to cross the TD (the crossing is demarcated by vertical lines in Fig. 2a), corresponding to a transition half-width of 49 000 km or $45\rho^{+}$. The magnetic field intensity profile shows a dip, down to $B^0 \approx 0.30$ nT; the field rotates over $|\omega| \approx 70°$. After transforming to the MVF, a relative velocity $\boldsymbol{V}_{\rm r} = (-10, +9)$ km s^{-1} is found. The normal velocity jump is 8 km s^{-1}; ideally, it should vanish for a TD. This value is indicative of the crudeness of the relative velocity approximation.

2.3. Event II

Fig. 3 shows the 2 s resolution magnetic field data in the MVF for a TD observed by ULYSSES on August 27, 1994, $05^{\rm h}37^{\rm m}$ UT, at 2.41 AU and $-78\overset{\circ}{.}2$ heliographic latitude; the TD is convected past ULYSSES with the solar wind emanating from the southern coronal hole (780 km s^{-1}). The ambient magnetic field is $B^{\infty} = 1.40$ nT. The proton density is $N^{\rm p} = 0.35$ cm^{-3} and the temperature $T^{\rm p}$ is 180 000 K (15.5 eV); these values vary less than 10 % in the vicinity of the transition. This implies a thermal proton velocity $V^{+}_{\rm th} = 55$ km s^{-1} and a gyroradius $\rho^{+} = 406$ km in the background magnetic field. The density of alpha particles is 0.018 cm^{-3}, their temperature about 800 000 K (56 eV). The electron temperature was measured to be 90 000 K (6.3 eV). The plasma beta is inferred to be $\beta \approx 1.98$.

As the TD normal is inclined to the average solar wind flow by 41°, the normal velocity is 585 km s^{-1}. The time to cross the TD is about 100 s (the interval demarcated in Fig. 3a), which translates to a transition half-width of 29 000 km or $72\rho^{+}$. Within the transition, the magnetic field drops to $B^0 \approx 0.68$ nT, indicating a significant kinetic pressure enhancement. The magnetic field rotates over a large angle: $|\omega| \approx 140°$. Transforming the velocities into the MVF, one finds $\boldsymbol{V}_{\rm r} = (-21, +22)$ km s^{-1}. The residual normal velocity is about 1 km s^{-1}.

2.4. Event III

A third example, with a completely different type of hodogram, is given in Fig. 4 (10 s time resolution). ULYSSES observed this TD on August 26, 1994, $01^{\rm h}40^{\rm m}$ UT, at 2.42 AU and $-79\overset{\circ}{.}1$ heliographic latitude, i.e. nearly at its southernmost position above the Sun's south pole. The coronal hole wind flows at 780 km s^{-1}. The solar wind plasma consists at this point of 6.9 eV (80 000 K) electrons, 15.0 eV (180 000 K) protons (density 0.48 cm^{-3}), and 75 eV (900 000 K) alpha particles (density 0.020 cm^{-3}). The proton thermal velocity is $V^{+}_{\rm th} = 54$ km s^{-1}. The ambient magnetic field is $B^{\infty} = 1.29$ nT; the thermal proton gyroradius in the background magnetic field is $\rho^{+} = 430$ km. The plasma beta is $\beta \approx 3.04$.

The TD normal is inclined to the solar wind speed by an angle of 65°; the normal velocity is 340 km s^{-1}. The crossing lasted about 200 s (demarcated by vertical lines in Fig. 4a), corresponding to a transition half-width of 34 000 km or $80\rho^{+}$; this transition is very wide. The magnetic field magnitude within the transition is reduced by only a small fraction, of the order of 10 %. The net field rotation is also small: about 8°. However, within the transition the field rotates significantly over more than 20°. After transforming to the MVF, a relative velocity $\boldsymbol{V}_{\rm r} = (-2.5, -2.9)$ km s^{-1} is found; the residual normal velocity is 0.5 km s^{-1}. The observational error on such small velocities is important. Also, due to the rather small variations in the magnetic field, there is an additional uncertainty in the MVF orientation.

3. Kinetic description

In order to understand the fine-structure of TDs, characterized by spatial scales of the order of the gyroradii of the relevant particles, one has to rely on a kinetic description. An extensive review of the underlying theory may be found in (Roth et al. 1996). The key ingredients of a kinetic TD model are (a) the identification of the plasma populations and their macroscopic properties, and (b) a choice for the analytical form of the velocity distribution functions (VDFs) of these populations. When trying to apply a kinetic model in a particular situation, there remain a number of

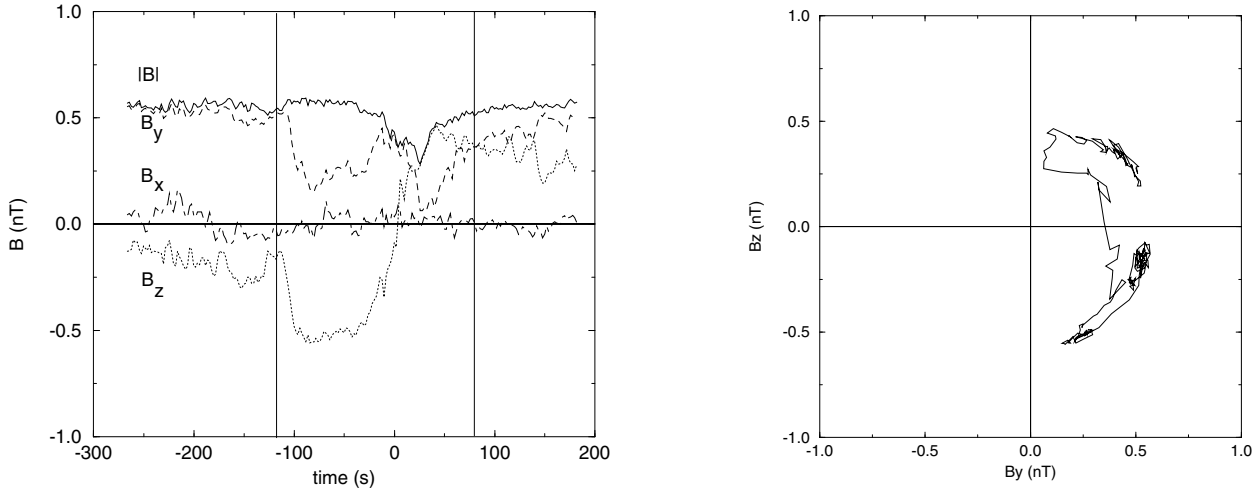

(a) (b)

Fig. 2a and b. Magnetic field profile observed by ULYSSES for event I. **a** The magnetic field components (2 s resolution) and magnetic field intensity are shown in the minimum variance frame. The time is given in seconds relative to 1993, July 3, $11^{\rm h}40^{\rm m}00^{\rm s}$. The passage is demarcated by the vertical lines and covers a normal TD distance of 98 000 km, corresponding to a TD half-width of $45\rho^+$. **b** Magnetic field hodogram during the TD passage, showing a rotation angle of 70°.

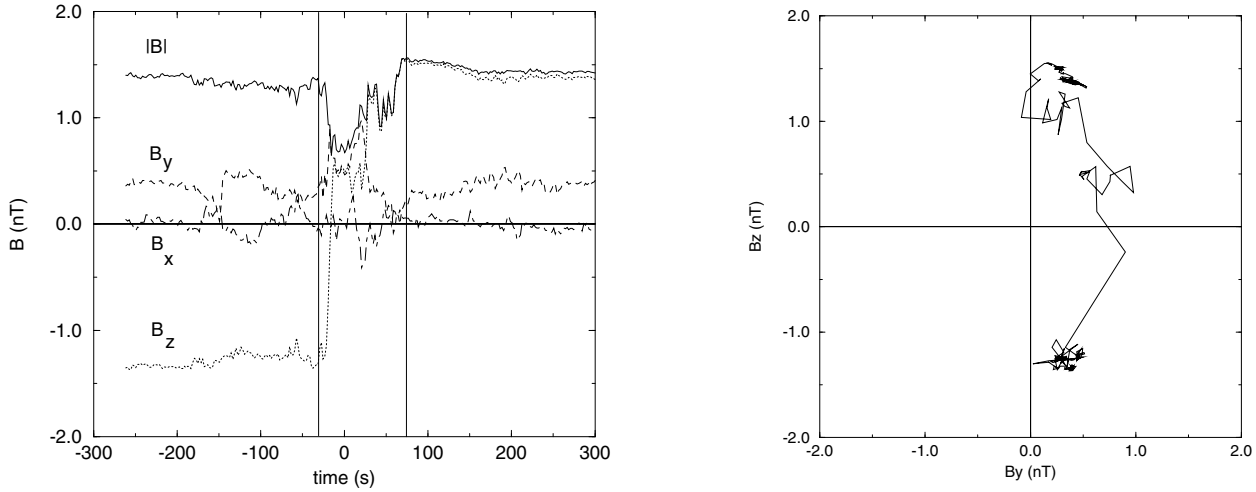

(a) (b)

Fig. 3a and b. Magnetic field profile observed by ULYSSES for event II. **a** The magnetic field components (2 s resolution) and magnetic field intensity are shown in the minimum variance frame. The time is given in seconds relative to 1994, August 27, $05^{\rm h}37^{\rm m}00^{\rm s}$. The demarcated crossing corresponds to a TD width of 58 000 km, or a half-width of $72\rho^+$. **b** Magnetic field hodogram, showing a large rotation of 140°.

unknowns: (a) not all macroscopic variables of the populations are known from direct measurements, and (b) there is a certain amount of arbitrariness in the choice of the form of the VDFs. Some of these unknowns can be related to structural properties of the TD, such as its width, but others remain essentially free in a plane TD model (Whipple et al. 1984). This arbitrariness can be resolved by tracing back the paths of particles in space or in time, or by making additional, physically reasonable, assumptions. The latter approach is taken here. The main free parameters in our model are the transition lengths, parameters used to describe the non-Maxwellian form of the VDFs inside the transition.

Sestero (1966) was one of the first to address the effect of the relative velocity on TD structure by means of kinetic theory. He focussed on a configuration without magnetic field rotation, where the relative velocity is perpendicular to the magnetic field

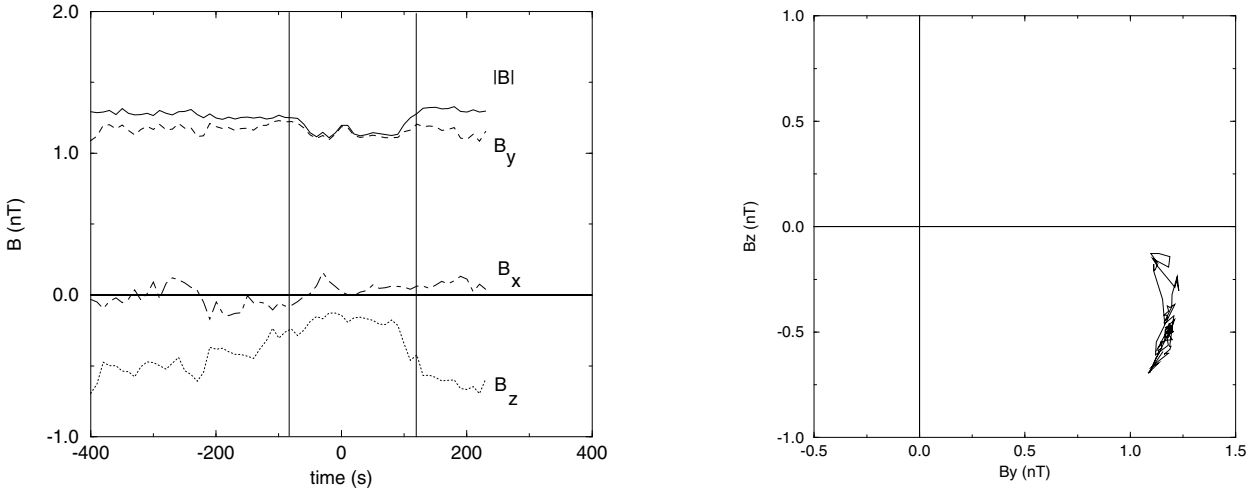

(a) (b)

Fig. 4a and b. Magnetic field profile observed by ULYSSES for event III. **a** The magnetic field components (10 s resolution) and magnetic field intensity are shown in the minimum variance frame. The time is given in seconds relative to 1994, August 26, $01^{\rm h}40^{\rm m}10^{\rm s}$. The TD width is 68 000 km, corresponding to a TD half-width of $80\rho^+$. **b** Magnetic field hodogram; because of the small rotation angle (8°) the paths traced by the tip of the magnetic field vector in the left and the right half of the transition nearly coincide.

direction, and concluded that there exist constraints on the orientation and magnitude of the relative velocity. A combination of Sestero's model with the Harris model (Harris 1962) was used by Kuznetsova et al. (1994) in a study of the stability of the high magnetic shear magnetopause when the relative velocity is anti-parallel to the magnetic field jump. The present paper generalizes these results by allowing a priori all possible magnetic field–relative velocity geometries and arbitrary magnetic field rotation angles.

3.1. Plasma populations

Our model includes electrons and protons only. This is a major simplification, as the alpha particles – with a number density of about 5 % of that of the protons – may well add up to 10 % of the currents and the total kinetic pressure. But for a qualitative understanding of equilibrium TD structure their contribution can be ignored.

We distinguish between "outer" and "inner" populations. The former are the only ones present far away from the transition; the latter have a nonzero density within the transition layer only. There are four outer populations: left and right electrons and protons. Because of plasma neutrality, their asymptotic densities must all be the same. Electron temperatures in the high speed solar wind tend to be lower than those of protons (Feldman et al. 1977; Maksimovic et al. 1995). Yet, it is assumed that electrons and protons have the same temperature T^∞, as this simplifies the kinetic analysis while not essentially altering TD structure.

In our model, an inner population is associated with each outer one. Inner populations can be thought of as being fed from the outer populations by a diffusion process that takes place on a sufficiently long time scale, thereby not endangering the validity of the collisionless equilibrium model. Their temperature is assumed to be identical to that of the outer populations. The maximum density of all inner populations ($N^{\rm i}$) is related to that of the corresponding outer populations (N^∞) by the same ratio $\nu = N^{\rm i}/N^\infty$. An inner population moves with a mean velocity which is the sum of the mean velocity of the corresponding outer population and an additional drift speed $\boldsymbol{V}_{\rm d}$. This is similar to the approach taken in (Kuznetsova et al. 1994). Our model requires protons and electrons to have opposite drifts $\boldsymbol{V}_{\rm d} = \boldsymbol{V}_{\rm d}^+ = -\boldsymbol{V}_{\rm d}^-$, like in the Harris model. Unlike the Harris model the orientation of the drift velocity component is not fixed, but remains a free parameter of the model. The diamagnetic drifts result in a current that is responsible for the rotation of the magnetic field; the current layer has a half-width of the order of $\mathscr{L}_{\rm H} = 2kT^\infty/eV_{\rm d}B^\infty$ (Harris 1962; Roth et al. 1996).

The resulting configuration is summarized in Fig. 5. There are 4 pairs of electron and proton populations: the outer left (OL), inner left (IL), inner right (IR) and outer right (OR) pairs.

3.2. Velocity distribution functions

The fact that populations can penetrate into the opposite half-space over only a limited distance implies an anisotropy in their VDF. As a particle of mass m, velocity $\boldsymbol{v}$ and charge Ze in a plane TD configuration is characterized by its three constants of motion, its energy $H = \frac{1}{2}mv^2 + Ze\phi$ and canonical momenta p_Y and p_Z ($\boldsymbol{p} = m\boldsymbol{v} + Ze\boldsymbol{a}$, where $\boldsymbol{a} = (0, a_Y(X), a_Z(X))$, $\boldsymbol{a}(0) = \boldsymbol{0}$ defines the magnetic vector potential), this non-Maxwellian behavior can be modelled by drawing a so-called cutoff line in the p_Y, p_Z plane in order to separate particles belonging to the left and the right side of the transition. This is represented

schematically in Fig. 6. The figure shows a projection of the phase space density onto the p_Y, p_Z plane at a given distance X from the center of the layer. The cutoff strongly reduces the particle density on one side of the line. As the relative position of the cutoff line and the bulk of the distribution depends on X, particles from a given population will remain on their proper side of the transition. The cutoff line is taken to be parallel to the diamagnetic drift velocity: its orientation is specified by the unit vector $\mathbf{1}_\mathrm{d} = -\boldsymbol{V}_\mathrm{d}/V_\mathrm{d}$. The abruptness of the cutoff is parameterized by a transition length $\mathscr{L}$.

One single form of VDF can describe both outer and inner populations (Roth et al. 1996). It is worthwhile to express the VDF in terms of the constants of motion, as it then automatically satisfies the Vlasov equation:

$$F = \eta(H, p_Y, p_Z) G(p_Y, p_Z).$$

This is a Maxwellian, centered around a mean velocity $\boldsymbol{V}$:

$$\eta = N\left(\frac{m}{2\pi k T^\infty}\right)^{\frac{3}{2}} \exp\left(-\frac{H}{kT^\infty} - \frac{mV^2}{2kT^\infty} + \frac{p_Y V_Y + p_Z V_Z}{kT^\infty}\right),$$

and modified by the cutoff factor

$$G = \left[C_1 \operatorname{erfc}(-U(p_Y, p_Z)) + C_2 \operatorname{erfc}(+U(p_Y, p_Z))\right]/2,$$

where

$$U = ((\boldsymbol{p} - m\boldsymbol{V}) \times \mathbf{1}_\mathrm{d})_X / ZeB^\infty \sqrt{\mathscr{L}^2 - \rho^2},$$

$$\rho = \sqrt{2mkT^\infty}/|Z|eB^\infty = mV_\mathrm{th}/|Z|eB^\infty,$$

with ρ being the gyroradius in the field B^∞. The cutoff function is parameterized by the characteristic transition length $\mathscr{L}$ ($\geq \rho$) and the orientation of the cutoff line $\mathbf{1}_\mathrm{d}$. The constants C_1 and C_2 indicate which half of the p_y, p_z space is allowed or forbidden. Fig. 6 corresponds to the values $C_1 = 0$ and $C_2 = 1$, removing particles from the region below the cutoff line. This choice represents the left populations; the right populations have $C_1 = 1$ and $C_2 = 0$.

A major property of multi-species transitions is whether they are associated with the non-Maxwellian nature of the VDFs of the ions (ion-dominated layers), or the electrons (electron-dominated layers), or both (mixed layers). Non-Maxwellian VDFs contribute in a particular way to the net current that is responsible for the magnetic field variation within the transition. Our model considers solar wind TDs to be mixed layers. The characteristic lengths $\mathscr{L}_+$ and $\mathscr{L}_-$ are taken to be the same for all proton resp. electron populations.

3.3. Electromagnetic structure

From the plasma neutrality condition (see appendix) it is found that $\phi(0) = 0$. The magnetic field intensity at the center of the transition can then be computed from the pressure balance condition for the plasma at ∞ and at 0:

$$B^0 = B^0_y = \pm\sqrt{1 - \nu\beta^\infty}, \tag{1}$$

where $\beta^\infty = 4\mu_0 N^\infty kT/(B^\infty)^2$. For a given β^∞ this equation implies a limitation on ν:

$$\nu \leq 1/\beta^\infty;$$

the inner population kinetic pressure should not exceed a certain limit, set by the magnetic pressure far from the TD.

The proposed VDF allows its moments, among which the partial densities n and currents $\boldsymbol{j}$, to be computed analytically by integrating over all particles of the population (Roth et al. 1996). This integration procedure is especially simple in the reference frame (x, y, z) shown in Fig. 7, which is obtained by rotation of (X, Y, Z) in the TD plane so as to align the positive y axis with the cutoff line direction $\mathbf{1}_\mathrm{d}$. It is convenient to introduce the following dimensionless quantities:

$$\tilde{x} = x/\rho^+, \quad \tilde{\boldsymbol{B}} = \boldsymbol{B}/B^\infty, \ \tilde{\boldsymbol{a}} = \boldsymbol{a}/\rho^+ B^\infty, \quad \tilde{\phi} = e\phi/kT^\infty,$$
$$\tilde{n} = n/N^\infty, \ \tilde{\boldsymbol{V}} = \boldsymbol{V}/V^+_\mathrm{th}, \ \tilde{\boldsymbol{j}} = \boldsymbol{j}/N^\infty e V^+_\mathrm{th}, \ \lambda_\pm = \rho^+/\mathscr{L}_\pm.$$

Henceforth, dimensionless quantities will be used and the tilde is dropped. The densities for all populations are:

$$\begin{aligned}
n^{\mathrm{ol}\pm} &= \mathrm{e}^{\mp(\phi + \boldsymbol{a}\cdot\boldsymbol{V}_\mathrm{r})} \operatorname{erfc}(-\lambda_\pm a_z)/2, \\
n^{\mathrm{or}\pm} &= \mathrm{e}^{\mp(\phi - \boldsymbol{a}\cdot\boldsymbol{V}_\mathrm{r})} \operatorname{erfc}(+\lambda_\pm a_z)/2, \\
n^{\mathrm{il}\pm} &= \nu \mathrm{e}^{2\boldsymbol{a}\cdot\boldsymbol{V}_\mathrm{d}} n^{\mathrm{ol}\pm}, \\
n^{\mathrm{ir}\pm} &= \nu \mathrm{e}^{2\boldsymbol{a}\cdot\boldsymbol{V}_\mathrm{d}} n^{\mathrm{or}\pm}.
\end{aligned} \tag{2}$$

Maxwell's equations lead to a system of 3 nonlinear second-order ODEs: Ampère's law for the magnetic vector potential components a_y and a_z, and Poisson's law for the electric potential ϕ. The latter ODE can be replaced by the (nonlinear) algebraic quasi-neutrality condition, which is a very good approximation (Roth et al. 1990). This equation allows ϕ to be computed explicitly when $\boldsymbol{a}$ is given; ϕ can thus be eliminated from the two remaining ODEs. As explained in the appendix, the Vlasov-Maxwell equations can be written in dimensionless form as:

$$a''_y + \beta^\infty\left[\frac{V_{ry}}{2} Q(\boldsymbol{a}) + V_{\mathrm{d}y} \bar{Q}(\boldsymbol{a})\right] = 0, \tag{3}$$

$$a''_z + \beta^\infty\left[\frac{V_{rz}}{2} Q(\boldsymbol{a}) + \hat{Q}(\boldsymbol{a})\right] = 0. \tag{4}$$

A solution is computed by numerical integration of Eqs. (3) and (4). Eq. (1) allows to find B^0 from the pressure balance condition. Given $\boldsymbol{a}(0) = \mathbf{0}$ and $\boldsymbol{a}'(0) = B^0(\sin\theta^0, -\cos\theta^0)$ (where θ^0 is the angle $\boldsymbol{B}(0)$ makes with the y axis) at the center of the transition, the integration procedure traces the solution backward to $-\infty$ and forward to $+\infty$. Numerical experiments indicate that, as V_r becomes larger, a critical value is reached above which the magnetic field component B_y no longer attains a fixed asymptotic value: no equilibrium solution satisfying the boundary conditions exists.

The computations are always carried out in the x, y, z frame, in which $\boldsymbol{V}_\mathrm{d}$ is along y. From the computed magnetic field profile, one subsequently finds the direction of the bisectrix of the asymptotic field vectors, and hence the X, Y, Z frame. In general, both frames do not coincide, and $\boldsymbol{V}_\mathrm{d}$ is not along Y.

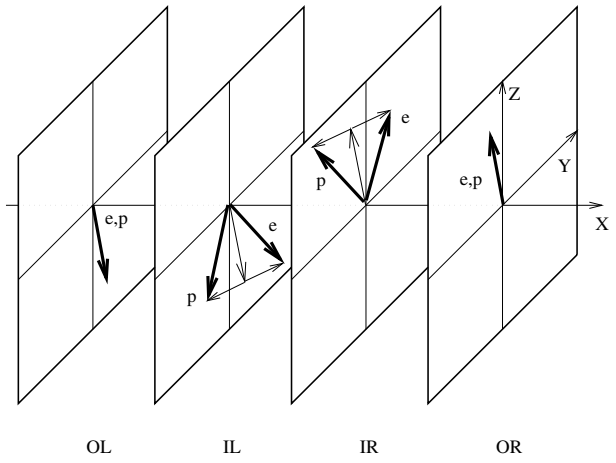

Fig. 5. Mean velocities of electron (e) and proton (p) populations in the (X, Y, Z) frame. The outer left proton and electron populations (OL+ and OL–) have the same mean velocity (equal to the asymptotic plasma bulk velocity), which is the opposite of that of the outer right populations (OR+ and OR–). The inner populations (IL+ and IL–, IR+ and IR–) have their diamagnetic drift superimposed on the mean velocity of the corresponding outer population; the drift velocity components of electrons and protons are opposite.

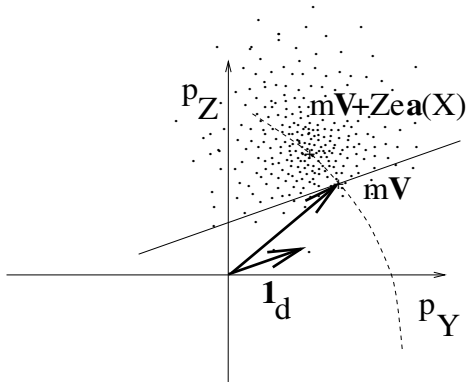

Fig. 6. Projection onto the p_Y, p_Z plane of the phase space density at a given position X inside the transition. The effect of the cutoff in the velocity distribution function manifests itself by an abrupt decrease of the phase space density on one side of the cutoff line oriented along $\mathbf{1}_\mathrm{d}$; which halfspace is selected depends on the choice of C_1 and C_2. This cutoff introduces an anisotropy in the VDF, which is responsible for the limited penetration of the population into the opposite halfspace: as X varies, the bulk of the distribution may be well above the cutoff line (purely Maxwellian distribution) or below it (vanishing density). The abruptness of the cutoff is controlled by the characteristic length and the typical gyroradius; it determines how deep a population can penetrate the opposite side of the TD, and thus affects the transition thickness.

The appendix presents an analysis of Maxwell's equations for $|x| < \min\{\mathscr{L}_\mathrm{H}, \mathscr{L}_+, \mathscr{L}_-\}$. This analysis shows how B_z linearly reverses its sign at the center of the transition; the sign of B'_z is the opposite of that of $V_{\mathrm{d}y}$, consistent with Harris' result (Harris 1962). The profile of B_y is approximately quadratic with x. Combining both equations, the magnetic field hodogram is found to have a parabolic shape at the transition center; the curvature of the parabola may be either way. This parabolic shape is evident in the observed hodograms, e.g. in Fig. 2b.

In the particular situation where no inner populations are present, the drift current is absent. The appendix shows that $a_y(x)$ and $a_z(x)$ then must be odd; hence $B_y(x)$ and $B_z(x)$ are even. Therefore, there is no net rotation across the transition, although the magnetic field may rotate significantly inside the TD layer. When $V_{\mathrm{r}y} = 0$, the magnetic field always points in the same direction throughout the transition, like in the Sestero case (Sestero 1966).

3.4. Existence domain

In this subsection we explore the domain of relative velocities for which our model allows an equilibrium configuration to exist.

Consider first the case $\boldsymbol{V}_\mathrm{r} \perp \mathbf{1}_\mathrm{d}$ (i.e. $V_{\mathrm{r}y} = 0$). It turns out that $a_y(x)$ is even and $a_z(x)$ is odd, so $B_y(x)$ is even while $B_z(x)$ is odd: the hodogram has mirror symmetry about the y axis, and the x, y, z and X, Y, Z frames coincide. We focus on the equation for a_z:

$$a''_z - \frac{\beta^\infty}{4}(1 + \nu \mathrm{e}^{2a_y V_{\mathrm{d}y}})\sinh(a_z V_{\mathrm{r}z}) A(a_z) = 0, \tag{5}$$

where the function $A(a_z)$ is given by:

$$A(a_z) = \frac{2}{\sqrt{\pi}}(\lambda_+ \mathrm{e}^{-\phi-\lambda_+^2 a_z^2} - \lambda_- \mathrm{e}^{\phi-\lambda_-^2 a_z^2}) - V_{\mathrm{r}z}(g_{\lambda_+}\mathrm{e}^{-\phi} + \hat{g}_{\lambda_-}\mathrm{e}^{\phi}).$$

Consider the situation where $\mathscr{L}_+ > \mathscr{L}_-$, $\lambda_+ < \lambda_-$. The behavior of $A(a_z)$ is then characterized for large arguments by

$$A(a_z) \approx \frac{2\lambda_+}{\sqrt{\pi}}\mathrm{e}^{-\lambda_+^2 a_z^2}, \quad |a_z| \quad \text{large},$$

consistent with $a''(\pm\infty) = 0$, and for small arguments by

$$A(a_z) \approx -2(V_{\mathrm{r}z} + \hat{V}_\mathrm{r}), \quad |a_z| \quad \text{small},$$

where

$$\hat{V}_\mathrm{r} = \frac{2}{\sqrt{\pi}}(\lambda_- - \lambda_+). \tag{6}$$

The $a_z(x)$ profile is found by integrating Eq. (5) starting from $a_z(0) = 0$. Given $\theta^0 = 0°$ (i.e. $B_y(0) > 0$), one has $\operatorname{sign} a'_z(x) = -\operatorname{sign} x$ close to the transition center. There are three possibilities:
(a) if $V_{\mathrm{r}z} > 0$ then $\operatorname{sign} a''_z(x) = +\operatorname{sign} x$,
(b) if $-\hat{V}_\mathrm{r} \le V_{\mathrm{r}z} \le 0$ then $\operatorname{sign} a''_z(x) = -\operatorname{sign} x$, and
(c) if $V_{\mathrm{r}z} < -\hat{V}_\mathrm{r}$ then $\operatorname{sign} a''_z(x) = +\operatorname{sign} x$.
In cases (a) and (c) the a_z profile may oscillate. In case (b) the B_y component will increase with x. Whatever the precise behavior of $A(a_z)$ for intermediate values of a_z, it is known to decrease

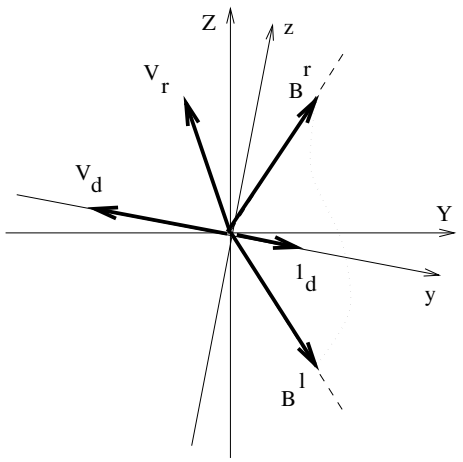

Fig. 7. Computations are performed most easily in a reference frame (x, y, z), which is such that the positive y axis coincides with the direction of the cutoff line $\mathbf{1}_\mathrm{d}$. In the model proposed in this paper, this is also the direction of $\boldsymbol{V}_\mathrm{d}$.

very fast as $|a_z|$ becomes large, and so one expects $B_y(x)$ to remain positive everywhere; a solution matching the boundary conditions can then always be found. A similar argument can be applied to the $\mathscr{L}_+ < \mathscr{L}_-$ case. In general, one finds:

$$\begin{array}{llll} B_y^0 > 0 & \mathscr{L}_+ \geq \mathscr{L}_- & -\hat{V}_\mathrm{r} \leq V_{\mathrm{r}z} \leq 0, \\ B_y^0 > 0 & \mathscr{L}_+ \leq \mathscr{L}_- & 0 \leq V_{\mathrm{r}z} \leq -\hat{V}_\mathrm{r}, \\ B_y^0 < 0 & \mathscr{L}_+ \geq \mathscr{L}_- & 0 \leq V_{\mathrm{r}z} \leq \hat{V}_\mathrm{r}, \\ B_y^0 < 0 & \mathscr{L}_+ \leq \mathscr{L}_- & \hat{V}_\mathrm{r} \leq V_{\mathrm{r}z} \leq 0. \end{array} \tag{7}$$

From the above line of reasoning it can be understood that

1. there exists a limit value $V_\mathrm{r}^\mathrm{max}$ of the order of $\hat{V}_\mathrm{r}$, beyond which no equilibrium solution can be found. As will be demonstrated in the examples, numerical simulation shows $\hat{V}_\mathrm{r}$ to be a lower bound for $V_\mathrm{r}^\mathrm{max}$. This result extends Sestero's informal conclusion for ion- and electron-dominated layers that the limit is of the order of the thermal velocity (Sestero 1966) to the case of mixed layers.
2. for a given magnetic field variation, there exists a preferential orientation for the relative velocity, the sense of which depends on the sign of the B_y^∞ component and on the characteristic lengths $\mathscr{L}_+$ and $\mathscr{L}_-$.

These conclusions also apply to the general case where $\boldsymbol{V}_\mathrm{r}$ has an arbitrary orientation. This is illustrated by the diagrams in Fig. 8. These diagrams have been computed for the typical values $\beta^\infty = 4$, $\theta^0 = 0°$, and $V_\mathrm{d} = 0.5V_\mathrm{th}^+$; they show which $\boldsymbol{V}_\mathrm{r}$ are compatible with a given magnetic field rotation $|\theta| = 90°$, i.e. for which $\boldsymbol{V}_\mathrm{r}$ a value of ν and an orientation of $\mathbf{1}_\mathrm{d}$ can be found such that a solution exists that meets the specified boundary conditions. These diagrams are given in the YZ plane, rather than in the yz plane, making it easier to relate the orientation of $\boldsymbol{V}_\mathrm{r}$ to the magnetic field jump $\Delta\boldsymbol{B}$. The contour in Fig. 8a outlines the existence domain for the case $\mathscr{L}_+ = 5\rho^+$ and $\mathscr{L}_- = \rho^+$. On the figure, the range $V_{\mathrm{r}Y} = 0$, $-\hat{V}_\mathrm{r} \leq V_{\mathrm{r}Z} \leq 0$ discussed above in case (b), is also indicated. From Eq. (6) one finds $\hat{V}_\mathrm{r} \approx 0.90V_\mathrm{th}^+$. The contour traces $\boldsymbol{V}_\mathrm{r}^\mathrm{max}$ for all directions in the YZ plane, thereby enclosing this range in agreement with the sufficient conditions (7). For the given sign of the B_Y^∞ component ($\theta^0 = 0°$ and $|\theta| < 180°$ imply that $B_Y^\infty > 0$) and for $\mathscr{L}_+ > \mathscr{L}_-$, the largest relative velocities are allowed when $V_{\mathrm{r}Z} < 0$. For the case $\mathscr{L}_+ < \mathscr{L}_-$, a similar diagram can be constructed; the largest relative velocities then correspond to $V_{\mathrm{r}Z} > 0$. Diagram 8b displays the case $\mathscr{L}_+ = \mathscr{L}_- = \mathscr{L} = 5\rho^+$.

Sestero gave a physical interpretation of the relative velocity limit. For a singly charged particle with kinetic energy $2kT$ on the left to penetrate over a distance of the order of a gyroradius into the right hand plasma, it has to overcome an energy barrier of ρeE. Roughly estimating the electric field E in the transition layer by the asymptotic convection electric field $V_\mathrm{r}B_y^\infty \approx V_\mathrm{r}B^\infty$ (if the rotation angle is not too large), he obtains $V_\mathrm{r} < 2kT/\rho eB^\infty = V_\mathrm{th}$.

3.5. Transition thickness

In this subsection an order-of-magnitude estimate of the transition thickness is derived. The transition half-width is defined as the distance $D = \rho^+ x$ at which the density of the outer left particles that penetrate into the right halfspace is reduced by a factor $\kappa = 10^{-2}$. The derivation is made for the right half of the transition, with $B_y^\mathrm{r} > 0$, $B_z^\mathrm{r} > 0$, $\boldsymbol{a} \cdot \boldsymbol{V}_\mathrm{r} < 0$ and $V_{\mathrm{d}y} < 0$. Let the angle between $\boldsymbol{B}^\mathrm{r}$ and the y axis be denoted by θ^r.

The width depends on the length scale $\mathscr{L}_\mathrm{H}$ of the spatial distribution of the inner populations, and on the interpenetration of the outer populations (effects related to the VDF anisotropy scales $\mathscr{L}_+$ and $\mathscr{L}_-$). The decay of the inner population density (see Eq. (2)) when moving away from the transition center is determined by $\mathrm{e}^{-2a_y|V_{\mathrm{d}y}|}$. A reduction by a factor κ corresponds to a half-thickness

$$x_\mathrm{H} \approx \frac{\operatorname{acosh}(\kappa^{-1/2})}{\sqrt{\nu\beta^\infty}V_{\mathrm{d}y}\sin\theta^\mathrm{r}} \approx \frac{3\mathscr{L}_\mathrm{H}}{\rho^+\sin\theta^\mathrm{r}}.$$

The left particle densities from Eq. (2) can be approximated for $x > 0$ by:

$$n^{\mathrm{o}1\pm} \approx \mathrm{e}^{\mp 2\boldsymbol{a}\cdot\boldsymbol{V}_\mathrm{r} - \lambda_\pm^2 a_z^2}/2\sqrt{\pi}\lambda_\pm|a_z|.$$

Closer inspection of this condition shows that the penetration of left ions into the right halfspace exceeds that of the electrons when $\boldsymbol{a} \cdot \boldsymbol{V}_\mathrm{r} < 0$ and $\lambda_+ \lesssim \lambda_-$, at least if the transition lengths are of the same order of magnitude.

Below, the situation $V_{\mathrm{r}y} = 0$ is considered in particular, i.e., the velocity difference is along the z axis and $\theta^\mathrm{r} = \theta/2$. Define the values $\xi^\pm = -\lambda_\pm a_z$ as the solutions of the nonlinear conditions

$$\mathrm{e}^{\pm 2\xi V_{\mathrm{r}z}/\lambda_\pm - \xi^2}/2\sqrt{\pi}\xi = \kappa.$$

As $|V_{\mathrm{r}z}/\lambda|$ cannot be much larger than 1 (see Eq. (6)), one finds that $0 \leq \xi^\pm \leq 3$. With $a_z \approx -B_y^\mathrm{r}x$, the penetration depths of ions and electrons are:

$$x_\pm \approx \frac{\xi^\pm(V_{\mathrm{r}z}/\lambda_\pm)}{\lambda_\pm \cos\theta^\mathrm{r}}.$$

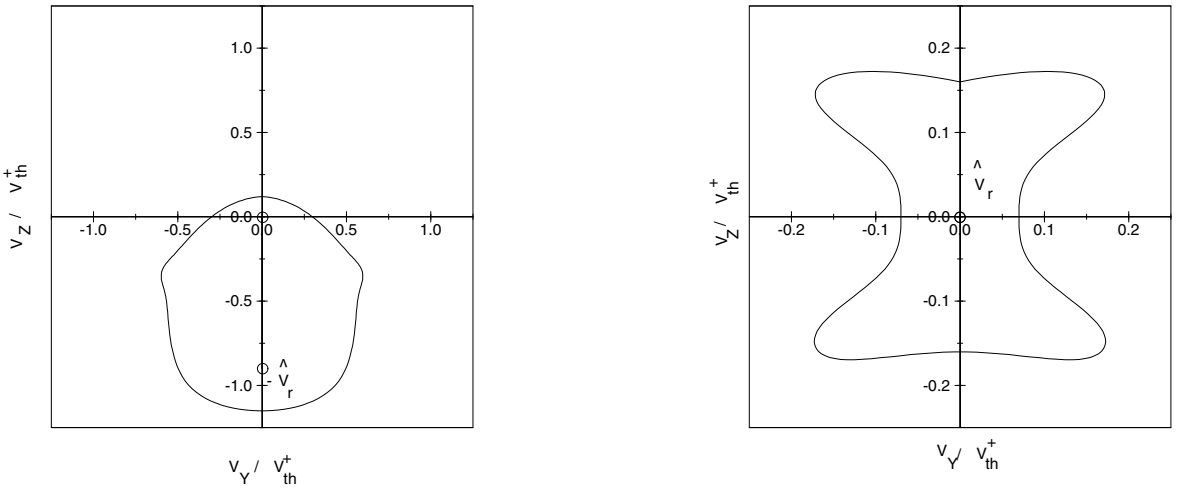

(a) (b)

Fig. 8a and b. Regions in the V_{rY},V_{rZ} plane where a solution exists for the typical values $\beta^{\infty} = 4$, $\theta^0 = 0°$, $V_{\rm d} = 0.5V_{\rm th}^+$, $|\theta| = 90°$. **a** Situation where the ion transition length is widest: $\mathscr{L}_+ = 5\rho^+$, $\mathscr{L}_- = \rho^+$, **b** Situation where ion and electron transition lengths are comparable: $\mathscr{L}_+ = 5\rho^+$, $\mathscr{L}_- = 5\rho^+$.

As $\xi_+(V_{{\rm r}z}/\lambda_\pm)$ is a monotonously increasing function of its argument, and as $\xi_+(V_{{\rm r}z}/\lambda_+) \approx \xi_-(-V_{{\rm r}z}/\lambda_-)$ when $\lambda_+ \approx \lambda_-$, this relation shows that ion penetration is strongest when $V_{{\rm r}z} > 0$; the electrons penetrate deepest when $V_{{\rm r}z} < 0$. This behavior must be ascribed to the role of the electric field in the layer, which is essentially the motional electric field: in the former case a positive electric field E_x repels the electrons, in the latter case a negative electric field prohibits left protons to enter the right side of the transition.

The half-width of the transition layer as a function of $V_{{\rm d}y}$ and $V_{{\rm r}z}$ (when $V_{{\rm r}y} = 0$) can be estimated by:

$$D \approx \max\{\frac{3\mathscr{L}_{\rm H}}{\sin(\theta/2)}, \frac{\xi^{\pm}(V_{{\rm r}z}/\lambda_\pm)\mathscr{L}_\pm}{\cos(\theta/2)}\}. \quad (8)$$

Both large and small magnetic field rotations (θ close to 0° resp. 180°) correspond to wide transitions, while a minimum thickness is obtained for $\theta \approx 90°$ if one assumes that $\mathscr{L}_+$, $\mathscr{L}_-$ and $\mathscr{L}_{\rm H}$ are of the same order.

4. Explaining the observed TD structure

Given the observed $\boldsymbol{B}^{\rm l}$ and $\boldsymbol{B}^{\rm r}$, $\boldsymbol{V}_{\rm r}$, and β^{∞}, the proposed kinetic model can be used to find matching values for ν, $\mathbf{1}_{\rm d}$, $V_{{\rm d}y}$, θ^0, $\mathscr{L}_+$ and $\mathscr{L}_-$. The ULYSSES high resolution magnetic field observations give additional information about the interior of the transition, thereby reducing the arbitrariness in the model. For instance, ν can be computed from B_y^0 by means of the pressure balance. The magnitude of the drift velocity $V_{\rm d}$ can be found from $\mathscr{L}_{\rm H}$, which can be measured in the field profile. For the relatively large rotations observed in events I and II, $\mathbf{1}_{\rm d}$ must be aligned more or less with the positive Y axis in the MVF, and θ^0 must be small. Thus, only matching $\mathscr{L}_+$ and $\mathscr{L}_-$ remain to be found. These values are not arbitrary either. As very narrow structure on the scale of the electron gyroradius is expected to be unstable, it is reasonable to assume that the characteristic lengths are both of the order of the proton gyroradius or larger. So, in conclusion, the parameters of the model are either fixed, or can be chosen within a limited range only. We now verify whether the observed magnetic field behavior for the three events is qualitatively compatible with the behavior predicted by the kinetic model.

4.1. Event I

Fig. 9 presents the simulation for event I. The top panels give the observations in the xyz frame (rotated clockwise over 25°, so that $\boldsymbol{V}_{\rm d}$ lies along y); the lower panels show the simulated profile and the hodogram in the same reference frame. Although the approximation is relatively crude, the overall structure of the transition is well reproduced by the simulation: the narrow but significant B_z reversal (corresponding to a large drift velocity $V_{{\rm d}y} = 10$ km s^{-1} and $\nu = 0.07$) embedded in a wider region with more or less symmetric B_y variations. The simulation used the values $\theta^0 = 5°$, $\mathscr{L}_+ = 5.15\rho^+$, $\mathscr{L}_- = 4.31\rho^+$, and a relative velocity $V_{\rm r}^{\rm sim} = 8.1$ km s^{-1}. The values of the characteristic lengths indicate that this transition should be modeled as a mixed type layer indeed: both proton and electron VDF anisotropies play a role. The relative velocity used in the simulation was somewhat smaller than the one derived from the observations: $V_{\rm r}^{\rm sim} = 8.1$ km s^{-1} $< V_{\rm r}^{\rm obs} = 13.5$ km s^{-1} (for larger $V_{\rm r}^{\rm sim}$ thinner layers were obtained). The diagram in Fig. 12a plots the points corresponding to $\boldsymbol{V}_{\rm r}^{\rm sim}$ and $\boldsymbol{V}_{\rm r}^{\rm obs}$. Recalling the uncertainty involved in the determination of $\boldsymbol{V}_{\rm r}^{\rm obs}$, the agreement in magnitude and orientation of the relative velocities used in the simulation and derived from observations is quite satisfactory.

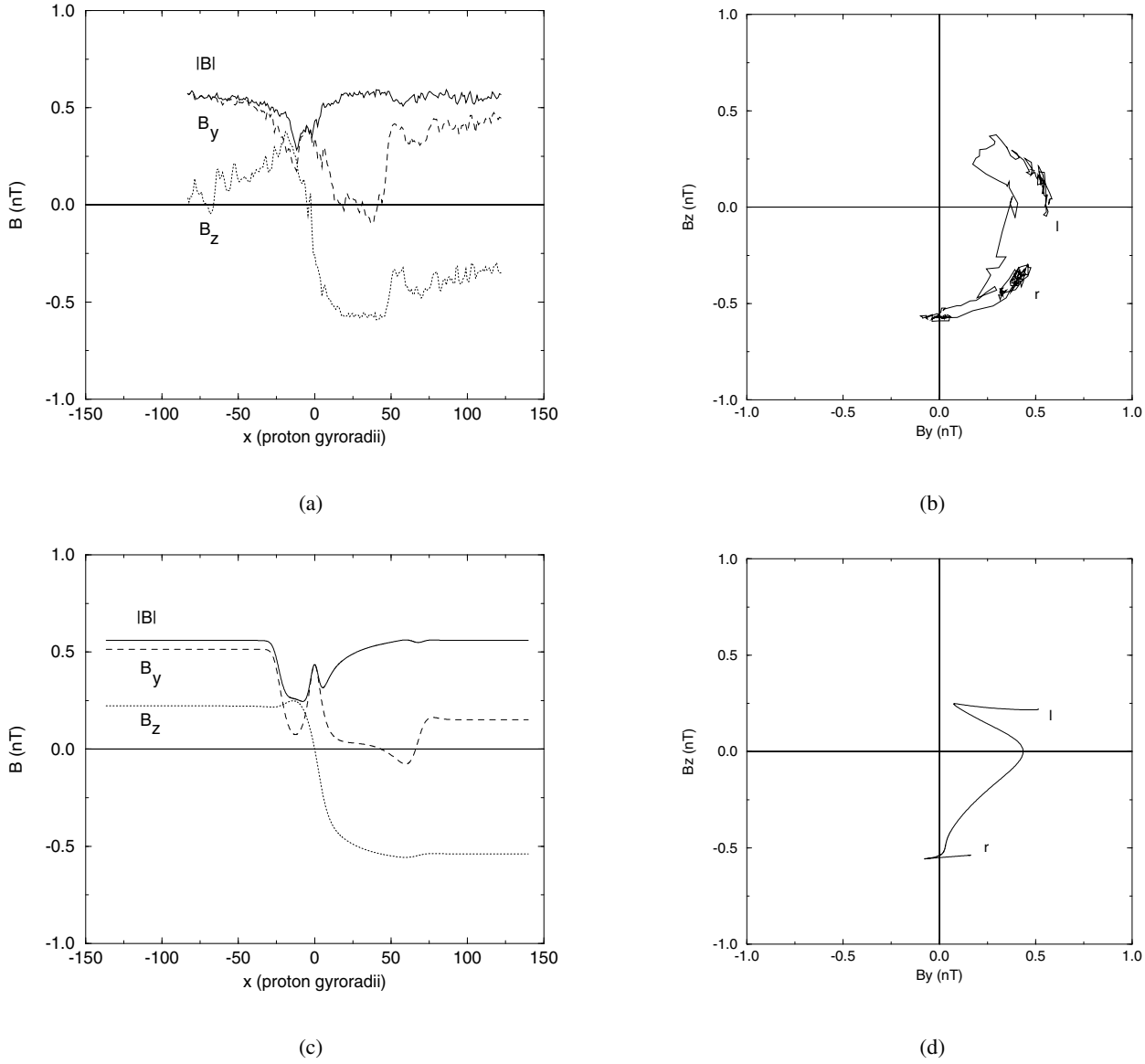

Fig. 9a–d. Simulation for event I. **a** Observed magnetic field profile in the xyz frame (MVF rotated clockwise over 25°). The normal distance x from the TD is expressed in proton gyroradii (ρ^+ = 1070 km). **b** Observed magnetic field hodogram in the xyz frame; l and r indicate the magnetic field vectors at the left resp. right side of the transition. **c** Simulated magnetic field profile. **d** Simulated hodogram.

Note also that $\boldsymbol{V}_{\rm r}^{\rm obs} \approx 0.24 V_{\rm th}^+$, i.e. the relative velocity is well below the thermal proton velocity, as the kinetic model requires. The situation corresponds qualitatively to the one depicted in Fig. 8b.

4.2. Event II

A simulation for event II is shown in Fig. 10. Again, the agreement is only qualitative. Especially the behavior at the right edge of the transition is poorly reproduced here. It is not surprising to see such deviations, as we attempt to model a structure with a width of the order of hundreds of gyroradii based on very simple assumptions regarding the inner populations. The simulation corresponds to: $\nu = 0.34$, $V_{{\rm d}y} = -1.25$ km s^{-1}, $\theta^0 = 30°$, $\mathscr{L}_+ = 5.2\rho^+$, $\mathscr{L}_- = 40\rho^+$, and a relative velocity $V_{\rm r}^{\rm sim} = 12.1$ km s^{-1} ($V_{\rm r}^{\rm obs} = 29$ km s^{-1} $= 0.54 V_{\rm th}^+$). The large value of ν is consistent with the large B_z variation and the large magnetic field rotation angle. In contrast to event I, the B_z reversal is more gradual, hence the lower drift velocity. The best matching configuration was found for a mixed layer with a large electron transition length. Roughly speaking, there is an ion-dominated layer embedded in a wider electron-dominated transition. Fig. 12b shows the matching orientations of $\boldsymbol{V}_{\rm r}^{\rm sim}$ and $\boldsymbol{V}_{\rm r}^{\rm obs}$, although their magnitudes are different. Note that the orientation of $\boldsymbol{V}_{\rm r}$ is consistent with the preferential direction discussed earlier for the case $\mathscr{L}_+ < \mathscr{L}_-$.

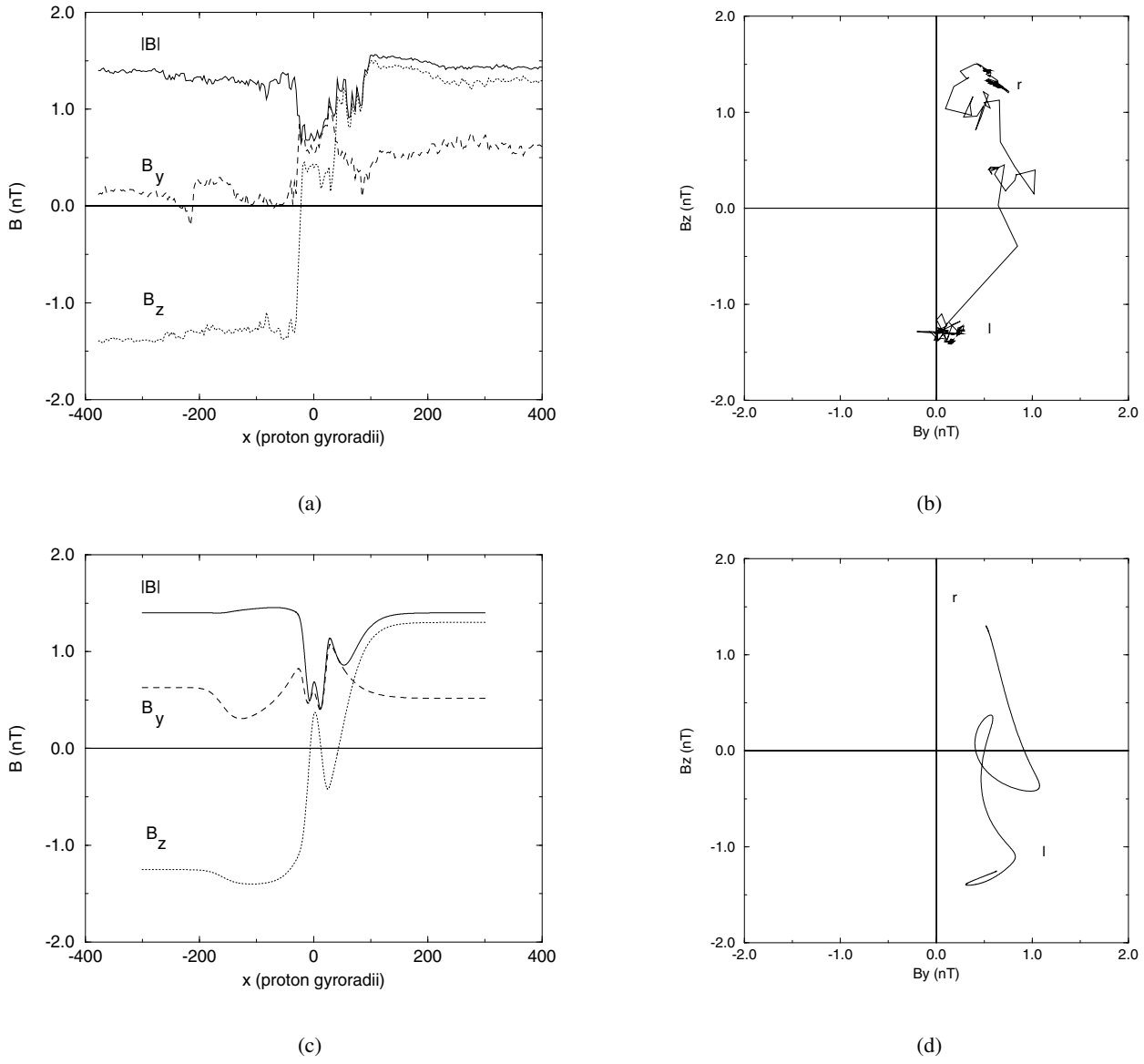

Fig. 10a–d. Simulation for event II. **a** Observed magnetic field profile in the xyz frame (MVF rotated clockwise over 10°). The normal distance x from the TD is expressed in proton gyroradii (ρ^+ = 406 km). **b** Observed magnetic field hodogram in the xyz frame; l and r indicate the magnetic field vectors at the left resp. right side of the transition. **c** Simulated magnetic field profile. **d** Simulated hodogram.

4.3. Event III

Event III is quite peculiar. It is, in fact, very close to the $\nu = 0$ case: the absence of inner populations and diamagnetic current leads to a transition with no net rotation. The B_z variations in the magnetic field profile are entirely due to the fact that $V_{ry} \neq 0$. In the simulation shown in Fig. 11 a small inner population ($\nu = 0.004$, $V_{dy} = -2$ km s^{-1}) has been added to account for the net field rotation of 8°. The simulation used $\theta^0 = 20°$, $\mathscr{L}_+ = 100\rho^+$, $\mathscr{L}_- = 18\rho^+$: the structure is very wide indeed. Note that the relative velocity required to establish this large solar wind structure is quite small: $V_r^{sim} = 3.0$ km s^{-1} ($V_r^{obs} = 3.8$ km s^{-1} $= 0.07V_{th}^+$). Again, as shown in diagram 12c, the orientations of $\boldsymbol{V}_r^{sim}$ and $\boldsymbol{V}_r^{obs}$ are consistent. There is again a correspondence with the preferential orientation illustrated in Fig. 8a.

5. Physical interpretation and conclusions

In this paper a kinetic model of mixed proton-electron TD transitions has been proposed to explore the relation between magnetic field rotation and the relative velocity between two plasmas on either side of a plane TD.

It was found that not any relative velocity is admissible; there exists an upper limit for the velocity difference the transition can support, and there is a preferential orientation. In particular, this preferential orientation depends on the nature of the transition, and is different in the $\mathscr{L}_+ > \mathscr{L}_-$ and $\mathscr{L}_+ < \mathscr{L}_-$ situations.

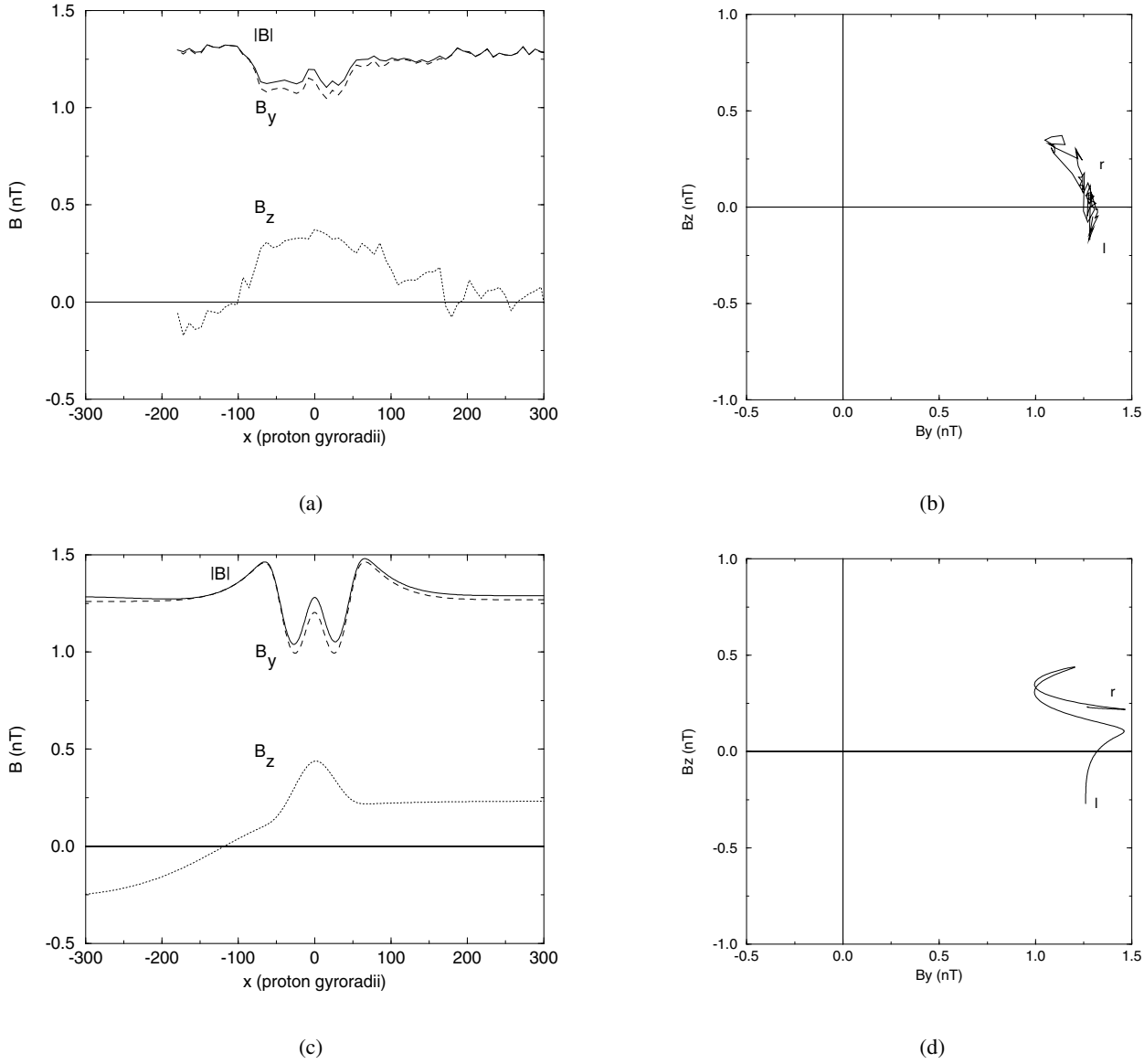

Fig. 11a–d. Simulation for event III. **a** Observed magnetic field profile in the xyz frame (MVF rotated counterclockwise over 25°). The normal distance x from the TD is expressed in proton gyroradii (ρ^+ = 430 km). **b** Observed magnetic field hodogram in the xyz frame; l and r indicate the magnetic field vectors at the left resp. right side of the transition. **c** Simulated magnetic field profile. **d** Simulated hodogram.

Numerical simulation was used to outline the feasible relative velocity domain. The relative velocity limit is of the order of the thermal velocity divided by the smallest characteristic length.

The magnetic field rotation angle depends on the inner population kinetic pressure: the absence of inner particles implies zero rotation (as witnessed by event III), a dense diamagnetic current sheet corresponds to a large rotation angle (as in event II). A relation has been established between the transition thickness and the magnetic field rotation angle: large rotation angles correspond to wide layers.

The overall behavior of the magnetic field variation can be approximated by the kinetic model, at least in a qualitative way. In particular, the correspondence of the morphology of the magnetic field profile and the orientation of the relative velocity between the observations and the simulation, indicates that the kinetic model is realistic.

Kinetic models, like the one proposed in this paper, rely on the introduction of morphological parameters, e.g. the characteristic transition lengths. Observations allow to estimate the values of these parameters, and hence to determine the nature of the transition: the cases discussed in this paper indicate that solar wind transitions should be considered to be mixed layers. The sometimes large values of the characteristic lengths indicate the presence of a diffusive physical process. The fact that $\mathscr{L}_-$ is of the order of the proton rather than the electron gyroradius, points out that such a process operates on the electrons in particular. The model also indicates that both characteristic lengths should not differ by a factor of more than 10; otherwise,

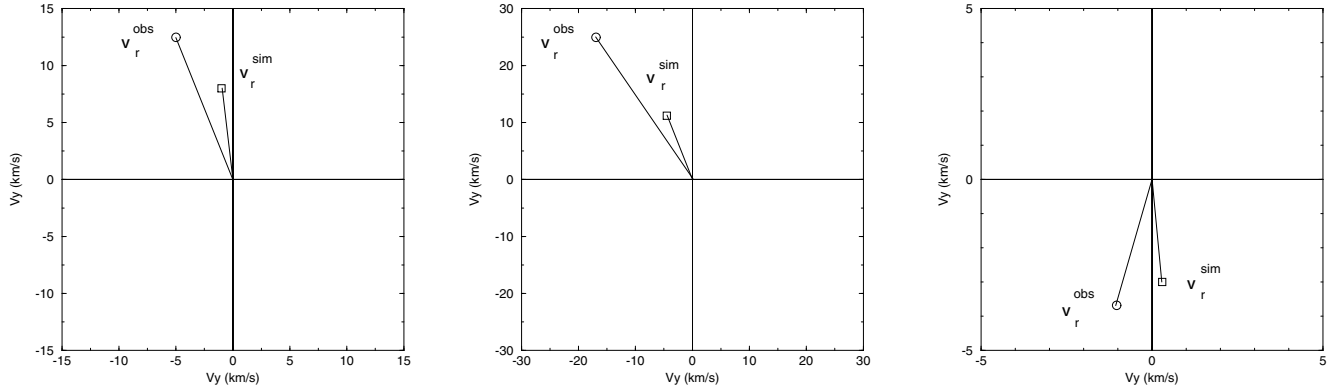

Fig. 12a–c. Relative velocities in the xyz frame. $\boldsymbol{V}_{\rm r}^{\rm obs}$ is the velocity jump inferred from the observations; $\boldsymbol{V}_{\rm r}^{\rm sim}$ is the velocity jump used in the simulation. **a** event I, **b** event II, **c** event III.

strong magnetic field gradients and localized electric fields are generated, which could easily initiate instabilities.

The case studies presented in this paper demonstrate that, in addition to temperature and density inhomogeneities in the solar wind, the non-constant bulk velocity is a major reason for the plasma to set up current-carrying boundary layers. It should be stressed that the few cases discussed in this paper not necessarily are representative for background solar wind TDs. In particular, due to the selectivity in the TD identification process, TDs associated with a rather large velocity jump are discussed here; those with low velocity jump may go unnoticed. It is therefore not surprising that all the presented events – in the framework of our model – seem to be at the edge of the existence domain, nor that they do match the preferential orientations apparent in Fig. 8.

The kinetic analysis and the restrictions on the relative velocity presented here refer only to equilibrium solutions; the effect of potential instabilities is not investigated. Instabilities (e.g., the Kelvin-Helmholtz instability) may impose additional restrictions on the relative velocity.

This paper dealt with transitions that have a rather simple internal structure. By stacking several simple transitions together, much thicker layers are obtained, across which larger velocity differences and magnetic field rotation angles are possible. The success of the model in explaining the structure of transitions with full widths of over a hundred proton gyroradii shows that stacking must not be advocated for regular solar wind TDs. HCS crossings, however, are known to be much wider (Behannon et al. 1981) and may have such a sandwich structure.

Other limitations of the proposed model discussed earlier include the planarity assumption, the fact that alpha particles are not accounted for, and the equal proton and electron temperatures. In spite of this, the model apparently is able to account at least qualitatively for a variety of observed transition profiles.

As evidenced by the simulations presented in this paper, a kinetic model is important in view of the interpretation of solar wind TD observations made by spacecraft in situ. The model itself, however, may have implications beyond solar wind research. For instance, TDs have also been observed at the magnetopause. There, a significant amount of field rotation is present together with an important relative velocity, as the magnetosheath plasma flows around the magnetosphere (Sonnerup & Cahill 1968; Berchem & Russell 1982a, 1982b). In this situation, important differences in plasma density and temperature on either side of the transition may exist (Eastman et al. 1996), except perhaps when there is a low-latitude boundary layer at the inner edge of the magnetopause (Phan & Paschmann 1996), requiring an extension of the proposed kinetic model; qualitatively speaking, however, the conclusions of the model should still hold.

Acknowledgements. The authors thank A. Balogh (Imperial College, London, England) for providing ULYSSES magnetic field data. They also thank J.F. Lemaire for his continuing support, and R. Lepping, A. Szabo and M.M. Kuznetsova for fruitful discussions. J.D.K. and M.R. are supported by the ESA (PRODEX) project "Interdisciplinary Study of Directional Discontinuities" as part of the ULYSSES mission, and acknowledge the support of the Belgian Federal Services for Scientific, Technological and Cultural Affairs. The research by B.T. and C.H. was carried out at the Jet Propulsion Laboratory, California Institute of Technology, under a contract with the National Aeronautics and Space Administration (USA). Work at Los Alamos was performed under the auspices of the U.S. Department of Energy with support from the NASA ULYSSES project.

Appendix

In this appendix, we derive the Vlasov-Maxwell equations in dimensionless form. Define the auxiliary functions:

$$
\begin{aligned}
f_\lambda(\boldsymbol{a},\boldsymbol{V}_{\rm r}) &= 1 - \mathrm{erf}\,(\lambda a_z)\tanh(\boldsymbol{a}\cdot\boldsymbol{V}_{\rm r}),\\
\hat{f}_\lambda(\boldsymbol{a},\boldsymbol{V}_{\rm r}) &= 1 + \mathrm{erf}\,(\lambda a_z)\tanh(\boldsymbol{a}\cdot\boldsymbol{V}_{\rm r}),\\
g_\lambda(\boldsymbol{a},\boldsymbol{V}_{\rm r}) &= 1 - \mathrm{erf}\,(\lambda a_z)\coth(\boldsymbol{a}\cdot\boldsymbol{V}_{\rm r}),\\
\hat{g}_\lambda(\boldsymbol{a},\boldsymbol{V}_{\rm r}) &= 1 + \mathrm{erf}\,(\lambda a_z)\coth(\boldsymbol{a}\cdot\boldsymbol{V}_{\rm r}).
\end{aligned}
$$

Quasi-neutrality can be translated into an expression for the electric potential $\phi(x)$:

$$e^{2\phi} = f_{\lambda_+}(\boldsymbol{a}, \boldsymbol{V}_r)/\hat{f}_{\lambda_-}(\boldsymbol{a}, \boldsymbol{V}_r).$$

Asymptotically, the behavior of the electric potential is determined exclusively by the convection electric field, while the potential is $\phi(0) = 0$ at the center of the transition. The expressions for the partial currents are:

$$\begin{aligned}
j_y^{\mathrm{lo}\pm} &= \mp\frac{1}{4}e^{\mp(\phi+\boldsymbol{a}\cdot\boldsymbol{V}_r)}\,\mathrm{erfc}\,(-\lambda_\pm a_z)V_{ry},\\
j_y^{\mathrm{li}\pm} &= \mp\frac{\nu}{4}e^{\mp(\phi+\boldsymbol{a}\cdot\boldsymbol{V}_r)-2\boldsymbol{a}\cdot\boldsymbol{V}_d}\,\mathrm{erfc}\,(-\lambda_\pm a_z)(V_{ry}\mp 2V_{dy}),\\
j_y^{\mathrm{ro}\pm} &= \pm\frac{1}{4}e^{\mp(\phi-\boldsymbol{a}\cdot\boldsymbol{V}_r)}\,\mathrm{erfc}\,(+\lambda_\pm a_z)V_{ry},\\
j_y^{\mathrm{ri}\pm} &= \pm\frac{\nu}{4}e^{\mp(\phi-\boldsymbol{a}\cdot\boldsymbol{V}_r)-2\boldsymbol{a}\cdot\boldsymbol{V}_d}\,\mathrm{erfc}\,(+\lambda_\pm a_z)(V_{ry}\pm 2V_{dy}),\\
j_z^{\mathrm{lo}\pm} &= e^{\mp(\phi+\boldsymbol{a}\cdot\boldsymbol{V}_r)}[\mp\frac{1}{4}\,\mathrm{erfc}\,(-\lambda_\pm a_z)V_{rz}+\frac{\lambda_\pm}{2\sqrt{\pi}}e^{-\lambda_\pm^2 a_z^2}],\\
j_z^{\mathrm{li}\pm} &= \nu e^{2\boldsymbol{a}\cdot\boldsymbol{V}_d} j_z^{\mathrm{lo}\pm},\\
j_z^{\mathrm{ro}\pm} &= e^{\mp(\phi-\boldsymbol{a}\cdot\boldsymbol{V}_r)}[\pm\frac{1}{4}\,\mathrm{erfc}\,(+\lambda_\pm a_z)V_{rz}-\frac{\lambda_\pm}{2\sqrt{\pi}}e^{-\lambda_\pm^2 a_z^2}],\\
j_z^{\mathrm{ri}\pm} &= \nu e^{2\boldsymbol{a}\cdot\boldsymbol{V}_d} j_z^{\mathrm{ro}\pm};
\end{aligned}$$

these expressions for the currents serve as source terms in Maxwell's equations, and one obtains:

$$a_y'' + \beta^\infty[\frac{V_{ry}}{2}Q(\boldsymbol{a}) + V_{dy}\bar{Q}(\boldsymbol{a})] = 0, \tag{A1}$$

$$a_z'' + \beta^\infty[\frac{V_{rz}}{2}Q(\boldsymbol{a}) + \hat{Q}(\boldsymbol{a})] = 0, \tag{A2}$$

where:

$$\begin{aligned}
Q(\boldsymbol{a}) &= \frac{1}{2}(1+\nu e^{2\boldsymbol{a}\cdot\boldsymbol{V}_d})\sinh(\boldsymbol{a}\cdot\boldsymbol{V}_r)[e^{-\phi}g_{\lambda_+} + e^{\phi}\hat{g}_{\lambda_-}],\\
\bar{Q}(\boldsymbol{a}) &= \frac{1}{2}\nu e^{2\boldsymbol{a}\cdot\boldsymbol{V}_d}\cosh(\boldsymbol{a}\cdot\boldsymbol{V}_r)[e^{-\phi}f_{\lambda_+} + e^{\phi}\hat{f}_{\lambda_-}],\\
\hat{Q}(\boldsymbol{a}) &= \frac{1}{2\sqrt{\pi}}(1+\nu e^{2\boldsymbol{a}\cdot\boldsymbol{V}_d})\sinh(\boldsymbol{a}\cdot\boldsymbol{V}_r)\\
&\qquad [\lambda_- e^{\phi-\lambda_-^2 a_z^2} - \lambda_+ e^{-\phi-\lambda_+^2 a_z^2}].
\end{aligned}$$

For $|x| < \min\{\mathscr{L}_H, \mathscr{L}_+, \mathscr{L}_-\}$ and $\theta^0 = 0°$, one finds:

$$\begin{aligned}
a_y(x) &\approx 0, \qquad a_z(x) \approx -B_y^0 x,\\
f_\lambda(x) &\approx 1 - \frac{2\lambda}{\sqrt{\pi}}V_{rz}a_z^2, \qquad g_\lambda(x) \approx 1 - \frac{2\lambda}{\sqrt{\pi V_{rz}}},\\
\hat{f}_\lambda(x) &\approx 1 + \frac{2\lambda}{\sqrt{\pi}}V_{rz}a_z^2, \qquad \hat{g}_\lambda(x) \approx 1 + \frac{2\lambda}{\sqrt{\pi V_{rz}}}.
\end{aligned}$$

Maxwell's equations (A1) and (A2) are simplified to:

$$a_y''(x) + \nu\beta^\infty V_{dy} \approx 0,$$

$$a_z''(x) + \frac{\beta^\infty}{2}(1+\nu)V_{rz}(V_{rz}+\hat{V}_r)a_z \approx 0,$$

with $\hat{V}_r$ as defined in Eq. (6). The magnetic field then is:

$$B_z(x) \approx -\nu\beta^\infty V_{dy}x, \tag{A3}$$

$$B_y(x) \approx B_y^0[1 - \frac{\beta^\infty}{4}(1+\nu)V_{rz}(V_{rz}+\hat{V}_r)x^2]. \tag{A4}$$

From (A3) and (A4) one can conclude that the magnetic field hodogram is parabolic at the center.

In the absence of inner populations, Maxwell's equations show that a_y'' and a_z'' are odd functions of $\boldsymbol{a}$, and f, $\hat{f}$, g and $\hat{g}$ are all even functions of $\boldsymbol{a}$. When $\theta^0 = 0°$ and $\boldsymbol{a}(0) = \boldsymbol{0}$, it follows that $a_y(x)$ and $a_z(x)$, and hence also $B_y(x)$ and $B_z(x)$, must be even: there is no net magnetic field rotation.

For large ν the ratio $|a_z/a_y|$ is small. The Vlasov-Maxwell equations can then be approximated up to moderate x values by:

$$a_y \approx -\frac{1}{V_{dy}}\ln\cosh(\sqrt{\nu\beta^\infty}V_d x), \tag{A5}$$

$$a_z'' - (1 + \frac{\nu}{\cosh^2(\sqrt{\nu\beta^\infty}V_d x)})\frac{\beta^\infty}{2}V_{rz}(V_{rz}+\hat{V}_r)a_z \approx 0. \tag{A6}$$

Eq. (A5) shows that in dense current sheets, where $\nu\beta^\infty \approx 1$, these equations describe a field reversal with a width determined by

$$\frac{\rho^+ V_{th}^+}{\sqrt{\nu\beta^\infty}V_d} \approx \frac{2kT^\infty}{eV_d B^\infty} = \mathscr{L}_H,$$

i.e. the half-width derived in the Harris model.

References

Bame, S. J., et al., 1992, A&AS, 92, 273

Behannon, K. W., Neubauer, F. M., Barnstorf, H., 1981, J. Geophys. Res., 86, 3273

Berchem, J., Russell, C. T., 1982a, J. Geophys. Res., 87, 2108

Berchem, J., Russell, C. T., 1982b, J. Geophys. Res., 87, 8139

Burlaga, L. F., Lemaire, J. F., Turner, J. M., 1977, J. Geophys. Res., 82, 3191

De Keyser, J., Roth, M., Lemaire, J.L., Tsurutani, B. T., Ho, C. M., Hammond, C. M., 1996, Solar Phys., 166, 415

Eastman, T.E., Fuselier, S.A., Gosling, J.T., 1996, J. Geophys. Res., 101, 49

Feldman, W.C, Asbridge, J.R., Bame, S.J., Gosling, J.T., 1977, in O.R. White (ed.), The Solar Output and its Variations, Colorado Associated University Press, Boulder, Colorado, USA, 351

Gosling, J. T., Hildner, E., Asbridge, J. R., Bame, S. J., Feldman, W. C., 1977, J. Geophys. Res., 82, 5005

Harris, E. G., 1962, Nuovo Cimento, 23, 115

Ho, C. M., Tsurutani, B. T., Goldstein, B. E., Phillips, J. L., Balogh, A., 1995, Geophys. Res. Lett., 22, 3409

Hudson, P. D., 1971, Planet. Space Sci., 18, 1611

Kuznetsova, M. M., Roth, M., Wang, Z., Ashour-Abdalla, M., 1994, J. Geophys. Res., 99, 4095

Lemaire, J. L., Burlaga, L. F., 1976, Ap&SS, 45, 303

Lepping, R. P., Behannon, K. W., 1986, J. Geophys. Res., 91, 8725

Maksimovic, M., Hoang, S., Bougeret, J.-L., 1995, in: Proceedings of the International Solar Wind 8 Conference

Phan, T.D., Paschmann, G., 1996, J. Geophys. Res., 101, 7801
Roth, M., 1986, in R. G. Marsden (ed.), The Sun and the Heliosphere in Three Dimensions, ASSL123, D. Reidel Publ. Co., Dordrecht, 167
Roth, M., Lemaire, J., Misson, A., 1990, J. Comput. Phys., 86, 466
Roth, M., De Keyser, J., Kuznetsova, M. M., 1996, Space Sci. Rev., 76, 251
Sestero, A., 1964, Phys. Fluids, 7, 44
Sestero, A., 1966, Phys. Fluids, 9, 2006
Sonnerup, B.U.Ö, Cahill, L.J., 1968, J. Geophys. Res., 73, 1757
Tsurutani, B. T., Smith, E. J., 1979, J. Geophys. Res., 84, 2773
Tsurutani, B. T., Ho, C. M., Smith, E. J., Neugebauer, M., Goldstein, B. E., Mok, J. S., Arballo, J. K., Balogh, A., Southwood, D. J., Feldman, W. C., 1994, Geophys. Res. Lett., 21, 2267
Whipple, E. C., Hill, J. R., Nichols, J. D., 1984, J. Geophys. Res., 89, 1508

This article was processed by the author using Springer-Verlag LaTeX A&A style file *L-AA* version 3.